DR. MATTHIAS GEYER (Orcid ID : 0000-0002-7718-5002)

Received Date : 19-Apr-2020

Revised Date : 17-May-2020

Accepted Date : 01-Jun-2020

Article type : Research Letter

Crystal structure of the human NLRP9 pyrin domain suggests a distinct mode of inflammasome assembly

Michael Marleaux[1], Kanchan Anand[1], Eicke Latz[2] and Matthias Geyer[1]

[1] Institute of Structural Biology, University of Bonn, Venusberg Campus 1, 53127 Bonn, Germany

[2] Institute of Innate Immunity, University of Bonn, Venusberg Campus 1, 53127 Bonn, Germany

Correspondence
Matthias Geyer
Institute of Structural Biology
Biomedical Center (BMZ)
University of Bonn
Venusberg Campus 1
53127 Bonn, Germany
Tel: +49 228 287 51400
E-mail: matthias.geyer@uni-bonn.de

Abbreviation
GSH, glutathione; GST, glutathione S-transferase; PYD, pyrin domain.

Abstract

Inflammasomes are cytosolic multimeric signaling complexes of the innate immune system that induce activation of caspases. The NOD-like receptor NLRP9 recruits the adaptor protein ASC to form an ASC-dependent inflammasome to limit rotaviral replication in intestinal epithelial cells, but only little is known about the molecular mechanisms regulating and driving its assembly. Here, we present the crystal structure of the human NLRP9 pyrin domain. We show that NLRP9^{PYD} is not able to self-polymerize nor to nucleate ASC specks in HEK293T cells. Comparison with filament forming pyrin domains revealed that NLRP9^{PYD} adopts a conformation compatible with filament formation but several charge inversions of interfacing residues might cause repulsive effects that prohibit self-oligomerization. These results propose that inflammasome assembly of NLRP9 might differ largely from what we know of other inflammasomes.

Keywords: NLRP9; PYD; structure; filament; ASC specks; inflammasomes

Introduction

The innate immune system comprises germline-encoded pattern recognition receptors (PRRs) that have evolved to directly recognize a wide range of conserved pathogen-associated molecular patterns (PAMPs), danger-associated molecular patterns (DAMPs), and homeostasis-altering molecular processes (HAMPs)[1]. They fulfill diverse functions with importance not only in pathogen recognition but also in tissue homeostasis, apoptosis, graft-versus-host disease, early development, and even negative regulation of inflammatory responses[2]. In the human immune system, PRRs group into five families, including Toll-like receptors (TLRs), RIG-I-like receptors (RLRs), C-type lectin receptors (CLRs), AIM2-like receptors (ALRs), and NOD-like receptors (NLRs). Of these PRRs, ALRs and certain NLRs were found to oligomerize upon ligand stimulation and participate in the formation of cytosolic multimeric signaling complexes, called inflammasomes[3]. Canonical inflammasomes translate and amplify signals from the PRR via an adaptor protein to activate the downstream effector cysteine protease caspase-1, which in turn processes the highly proinflammatory cytokines pro-IL-1β and pro-IL-18 into their mature forms[4,5]. Active caspase-1 also cleaves gasdermin D to induce pore formation in the host cell for the

release of cytokines and pyroptotic cell death[5,6]. Notably, signal amplification is facilitated by unified nucleation-driven polymerization of the individual inflammasome components[7–9]. As an example, NLRP3 is an inflammasomal sensor protein that belongs to a subfamily of NLRs (termed NLRPs) containing an N-terminal pyrin domain. After an initial priming step and activation by a wide range of diverse stimuli, it recruits the bipartite protein 'apoptosis-associated speck-like protein containing a caspase recruitment domain' (ASC) as an adaptor for caspase-1 activation[8,10–12]. NLRP3 polymerizes with its pyrin domain (PYD) to form the nucleation seed for ASC filament assembly using three major types of asymmetric interfaces, which has also been described for NLRP6 and AIM2[7,13–15]. ASC filaments in turn nucleate the formation of large caspase-1 filaments by caspase activation and recruitment domain (CARD)/CARD interactions, which finally leads to proximity-induced autoproteolytic activation of caspase-1[7]. Therefore, inflammasome assembly significantly relies on homotypic interactions between PYD- and CARD-domains of the respective components.

A less studied member of the NLRP subfamily is NLRP9, which was first described as a maternal effect gene in bovine[16–19]. Upon recognition of low molecular weight dsRNA by the endogenous RNA helicase DHX9, its mouse analogue NLRP9b was described to form an inflammasome with ASC and caspase-1[20,21]. This inflammasomal complex mediates pyroptosis of intestinal epithelial cells, thereby limiting rotaviral replication in mice[20,21]. Additionally, NLRP9b deficiency resulted in less pulmonary histopathological alterations in a mouse model of acute lung injury and markedly elevated proinflammatory cytokine and chemokine levels, as well as ROS production, in a LPS-activated mouse epithelial cell line[22]. Also, expression of NLRP9 in human intestinal epithelial cells and DHX9-dependent association with ASC upon stimulation with rotavirus could be shown[21]. Moreover, upregulation of expression was found upon inflammatory stimuli ROS and interferon-γ in brain pericytes and cerebral endothelial cells, respectively[23,24]. However, the role of human NLRP9 in innate immunity is not yet clarified and elucidation of its inflammasome function would be valuable. This holds particularly true, as alterations in NLRP9 expression were linked to several inflammatory diseases, including urothelial carcinoma, multiple sclerosis, juvenile idiopathic arthritis, familial late onset Alzheimer disease, and infection with *Helicobacter pylori*[25–31].

To gain first insights into NLRP9 inflammasome assembly, we expressed and purified recombinant human NLRP9^{PYD} and studied its capability to self-polymerize into filaments and nucleate ASC speck formation. We found that NLRP9^{PYD} exists as a monomer under near physiological conditions *in vitro* and in cells. In contrast to NLRP3^{PYD}, overexpression of murine or human NLRP9^{PYD} did not nucleate ASC speck formation in HEK293T cells. We determined the crystal structure of human NLRP9^{PYD} to study the molecular differences from filament forming pyrin domains and discuss its implications for the assembly of the NLRP9 inflammasome.

Materials and methods

Cloning, expression, and purification of the human NLRP9 pyrin domain

The coding sequence of a human NLRP9 cDNA clone (GenBank accession NM_176820) corresponding to residues 1–97 was amplified by PCR with specific oligonucleotides encompassing *Nco*I/*Eco*RI restriction sites at the 5' and 3' end, respectively. The DNA product was cloned into a modified pGEX-4T-1 vector carrying an N-terminal Glutathione S-Transferase (GST) tag for affinity purification followed by a tobacco etch virus (TEV) protease cleavage site. The expression construct was confirmed by DNA sequencing and transformed into *Escherichia coli* BL21(DE3) cells. Expression cultures were initially grown at 37°C in LB medium, supplemented with 100 mg/L Ampicillin. When OD_{600} reached 0.8, cells were cooled to 16°C before protein expression was induced by addition of 0.55 mM isopropyl-β-D-thiogalactopyranoside (IPTG). Bacteria were further grown over night at 16°C, harvested by centrifugation and stored at -80°C.

For purification, cells were resuspended in buffer A (50 mM HEPES pH 7.5, 150 mM NaCl and 10 mM βME) containing 1 mM phenylmethylsulfonylfluoride (PMSF), and 1 mg/L DNAse I, and lysed by the addition of lysozyme and further sonication. The lysate was cleared from cell debris by centrifugation at 70,000 x g for 30 minutes. The protein containing an N-terminal GST tag was captured using a GSTrap column (GE Healthcare) and the unbound fraction was washed off with buffer B (50 mM HEPES pH 7.5, 300 mM NaCl, 10 mM βME), followed by buffer A. After elution with buffer A containing 10 mM reduced glutathione, the GST tag was cleaved off overnight at 4°C by the addition of 1:100 w/w TEV protease. Protein was further purified using a Superdex 75 gel filtration column 16/600 (GE Healthcare) that was connected to a GSTrap column for prolonged retention of the cleaved GST tag and pre-equilibrated with buffer C (50 mM HEPES pH 7.5, 150 mM NaCl, 1 mM TCEP). Peak fractions containing $NLRP9^{PYD}$ were pooled, concentrated to 31.7 mg/ml, snap frozen in liquid nitrogen, and stored at -80°C.

Crystallization and diffraction data collection

Protein solution was crystallized by the hanging drop vapor diffusion method at 15°C. Initial crystals were obtained by JCSG+ screen[32] (0.2 M potassium formate, 20% PEG3350). The optimal hexagonal-shaped crystals were grown with 1:1 ratio of protein and precipitant solution by using 0.1 M Bicine pH 9.0, 0.2 M sodium thiocyanate, 0.1 M sodium formate, and 25-27% v/w PEG3350. Crystals were cryo-protected with 15% ethylene glycol in the mother-liquor and flash cooled in liquid nitrogen.

Data were collected at the synchrotron beamlines of Swiss Light Source (SLS) in Villigen,

Switzerland, and Deutsches Elektronen Synchrotron (DESY) in Hamburg, Germany. Presented diffraction data up to 1.95 Å resolution were collected from native crystals at 100K on the X-ray diffraction PX1 beamline using Eiger detector at SLS.

Data processing, structure determination and refinement

Data were processed and scaled using the XDS program package[33]. The phase problem was solved by molecular replacement method[34] using program PHASER[35] and the coordinates of NLRP4^{PYD} (4EWI)[36] as a search model for the phase solution. The model was refined in alternating cycles of refinement with PHENIX[37]. Manual rebuilding and visual comparisons were made using graphical program COOT[38]. The stereo chemical quality of the model was verified using Ramachandran plot. Molecular diagrams were drawn using the PyMOL molecular graphics suite[39]. The final model contains residues 9–97 and has been refined to R_{work} and R_{free} values of 21.5% and 22.2%, respectively. Details of the diffraction data collection, quality, and refinement statistics are given in Table 1. The atomic coordinates and structure factor amplitudes have been deposited in the Protein Data Bank with accession code 6Z2G.

Dynamic Light Scattering

The protein was diluted to 2 mg/ml in buffer C and prepared for dynamic light scattering (DLS) by centrifugation at 18,000 x g for 10 minutes. The supernatant was incubated for 11.5 h at 25°C and the size distribution of the sample was measured every 30 minutes using a DynaPro NanoStar (Wyatt Technology) set to an acquisition time of 3 seconds. Each data point was averaged from 20 DLS acquisitions. The cumulant analysis and calculation of the hydrodynamic radius (r_H) and molecular weight of the protein was automatically performed by the software supplied with the instrument (Dynamics 7.8.3).

Analytical gel filtration

50 µg of the protein that was prepared for dynamic light scattering was loaded before and after incubation for 12 h at 25°C onto a 1260 Infinity II LC system connected to a Superdex 75 analytical gel filtration column 3.2/300 (GE Healthcare) that was pre-equilibrated with buffer C. Gel filtration standard (BioRad) was used according to the manufacturer's instructions to calculate a standard curve and determine the molecular weight of the protein species.

Analysis of pyrin domain filament and ASC speck formation in cells

HEK293T cells or HEK293T cells stably expressing ASC-TagBFP under the CMV promoter (HEK293T$^{ASC\text{-}BFP}$) were seeded into 96 well plates and grown for 48 h. Per well, 200 ng of plasmid

DNA coding for the indicated fusion proteins or control was transfected with Lipofectamine 2000 according to manufacturer's instructions. 24 h after transfection, cells were fixed and simultaneously stained for nuclei using 4% formaldehyde plus 10 µM Draq5 diluted in PBS. Cells were imaged using a ZEISS Observer.Z1 epifluorescence microscope, equipped with 20x objective (dry, PlanApochromat, NA 0.8), Axiocam 506 mono, and software ZEN 2.3 Pro. For visualization, brightness and contrast were adjusted. Six images per experiment and condition were analyzed for filament or ASC speck formation using program CellProfiler[40]. In total, 3338, 938, 2398, and 2794 HEK293T cells and 4549, 1628, 3593, and 5350 HEK293T$^{ASC\text{-}BFP}$ cells positive for expression of either hNLRP3^{PYD}-mCitrine, hNLRP9^{PYD}-mCitrine, mNLRP9b^{PYD}-mCitrine, or the mCitrine vector control, respectively, were analyzed for filament and ASC speck formation. Plotting of graphs and calculation of statistics was performed using GraphPad Prism version 7.0e for Mac.

Results

Structure of the NLRP9 pyrin domain

NLRP9 consists of an N-terminal pyrin domain and a central NACHT domain similar to all NLRP proteins. The NACHT domain is directly followed by a C-terminal leucine rich repeat (LRR) domain that can be divided into a transition and a canonical LRR (Figure 1A). While the interplay of all different domains might be important for active inflammasome formation, pyrin domains of NLRP3, NLRP6, and AIM2 were found to form filaments and connect the inflammasome sensor with the adaptor protein ASC for caspase recruitment and activation[13–15]. To study the inflammasome assembly of NLRP9, we expressed human NLRP9^{PYD} as a GST-fusion protein in *Escherichia coli*. The protein was purified to homogeneity by affinity chromatography followed by tag cleavage and size exclusion chromatography at near physiological buffer conditions. NLRP9^{PYD} was readily concentrated up to 120 mg/ml without precipitation or aggregation. Consequently, we crystallized NLRP9^{PYD} for investigation of its structural features. Hexagonal-shaped crystals appeared in 0.1 M Bicine pH 9.0, 0.2 M sodium thiocyanate, 0.1 M sodium formate, 25-27% PEG3350 and diffracted up to 1.95 Å resolution using the PX1 beamline and Eiger detector at SLS. Initial phases were obtained by molecular replacement using the coordinates of the NLRP4^{PYD} crystal structure[36] with 59.6% sequence identity as search model. The protein structure was refined to R_{work} of 21.5% and R_{free} of 22.2% with excellent stereochemistry (Table 1). In the protein crystal, one monomer of NLRP9^{PYD} formed the

asymmetric unit (unit cell dimensions a = 33.33 Å, b = 33.33 Å, and c = 311.09 Å (Table 1)). In the final model of NLRP9^{PYD} residues 9-97 could be built into the electron density map (Figure 1B). The N-terminus region of the molecule that contributes to about 10% of the structure as well as several side chains facing towards solvent channels are disordered and could not be resolved by electron density, leading to a higher overall temperature factor of 68.96 Å^2 (Table 1, Figure 1B).

As other members of the death domain superfamily, NLRP9^{PYD} displayed six antiparallel helices, connected by five loops and arranged in the typical death domain fold[41] (Figure 1B). The helices are formed by residues 10-15 (α1), 20-31 (α2), 44-47 (α3), 52-62 (α4), 66-78 (α5), and 82-96 (α6). Of note, α3 is a short 3_{10}-helix. NLRP9^{PYD} contains polar residues at the surface, which were found to be of mainly basic character (Figure 1C). Residues with highest flexibility of backbone and sidechains were found at the N-terminus of α1, the C-terminus of α6, and within the α2-α3 loop (Figure 1D). In contrast, the overall fold of NLRP9^{PYD} is substantially stabilized by a central hydrophobic core with lower flexibility, which is formed by residues Leu15 of α1, Leu18 in the α1-α2 loop, Phe26 and Leu30 of α2, Ile42 in the α2-α3 loop, Leu47 of α3, Ala50 in the α3-α4 loop, Val55 and Leu59 of α4, Leu75 and Phe76 of α5, Ile79 in the α5-α6 loop, and Leu84 of α6 (Figure 1D, E). Hydrophobicity of the majority of those residues positioned in the central core of NLRP9^{PYD} was found to be conserved among other pyrin domains (Figure 3A), confirming their importance for domain stability. Similarly, the α2-α3 loop is stabilized by a second hydrophobic, but more flexible cluster formed by residues Leu34, Phe37, and Leu39 in the α2-α3 loop, Tyr63 in the α4-α5 loop, and Val71 of α5 (Figure 1E). The determined distribution of regions with lower and higher flexibility is equivalent for pyrin domains of other NLRPs[42–44]. However, the overall flexibility was found to be significantly higher in NLRP9^{PYD}, which prompted our further investigations.

NLRP9^{PYD} is monomeric and does not self-polymerize *in vitro*

Since pyrin domains of NLRP3, NLRP6, and AIM2 are able to form filaments[13–15], we asked whether NLRP9^{PYD} would also feature such ability. Our initial investigations by electron microscopy revealed that the protein did not tend to form filamentous structures under the tested conditions *in vitro*. Therefore, we set out to analyze its size distribution and experimental molecular weight during a 12 h incubation period at 25°C using dynamic light scattering and analytical gel filtration (Figure 2). We found that during incubation NLRP9^{PYD} particles have a stable average hydrodynamic radius of 1.7 nm, corresponding to a molecular weight of approximately 12 kDa (Figure 2A). Consistently, analytical gel filtration revealed an average molecular weight of 11.93 kDa for NLRP9^{PYD} independent of the incubation time (Figure 2B, C).

Since the theoretical molecular weight of monomeric NLRP9^{PYD} is 11.96 kDa, we concluded that NLRP9^{PYD} is monomeric in solution and does not self-polymerize *in vitro*.

Comparison of NLRP9^{PYD} with filament forming pyrin domains

Using our structural data, we next tried to understand the inability of NLRP9^{PYD} to form filaments on a molecular basis. To compare residues at positions that are typically involved in filament formation, we performed structure-based sequence alignments of the PYD of NLRP9 and the filament forming PYDs of NLRP3, NLRP6, AIM2, and ASC (Figure 3A). Assembly of pyrin domain filaments is dependent on the formation of three asymmetric interfaces, of which the type I interface mediates intra-strand interactions and type II and type III interfaces mediate inter-strand interactions[7,13,15] (Figure 3B). We supposed, that residues located in such interfaces and matching by charge or hydrophobicity in NLRP3, NLRP6, AIM2 or ASC pyrin domains might be mismatching in NLRP9^{PYD}. Indeed, we found several charge inversions in the proposed interfaces of NLRP9^{PYD} compared to the other four PYDs, such as Asp8, Lys16, Arg19, Lys20, Glu46, Lys48, Lys57, and Lys61 as well as charge insertions of otherwise hydrophobic residues, such as Glu28 and Glu53. Additionally, Phe9 and Trp24 were found as large hydrophobic insertions (Figure 3A). Although, the presumed mismatches could compensate each other in the interfaces, we speculate that some of them might disrupt NLRP9^{PYD} filament formation. Of note, NLRP3^{PYD}, NLRP6^{PYD}, AIM2^{PYD}, and ASC^{PYD} displayed sequence identities of 28.7%, 26.4%, 25.0% and 21.8% with NLRP9^{PYD}, respectively (residues 8-94, Figure 3A).

Given that pyrin domains can undergo large conformational changes upon formation of the filament[7,13,15], also residues outside of binding interfaces have to be considered for further analysis, since they might limit NLRP9^{PYD} to conformations incompatible with filament formation. In pyrin domains of NLRP6 and ASC, the position and rotation of the flexible α2-α3 loop together with its connecting α2- and α3-helices were found to undergo most prominent changes on filament formation[7,15]. Therefore, we analyzed those regions in the NLRP9^{PYD} structure and asked whether they would be able to adopt the filament conformation without steric hinderance. For this purpose, we overlaid NLRP9^{PYD} with monomeric and filamentous NLRP6^{PYD} (Figure 3C). Unexpectedly, we found NLRP9^{PYD} to superimpose better with the structure of NLRP6^{PYD} from the filament (RMSD of 1.2 Å) as if compared with monomeric NLRP6^{PYD} (RMSD of 1.6 Å). Indeed, especially the conformation of the α2-α3 loop region of NLRP9^{PYD} is highly similar to the filamentous NLRP6^{PYD} (Figure 3C). To further validate this finding, we aligned NLRP9^{PYD} with the less related monomeric and filamentous AIM2^{PYD} (Figure 3D), and ASC^{PYD} (Figure 3E). They superimposed to RMSD values of 1.1 Å and 1.7 Å for AIM2^{PYD}, and to 1.3 Å and 1.5 Å for ASC^{PYD}, respectively. However, intuitively the appearance of the α2-α3 loop region of NLRP9^{PYD}

seems to resemble the conformations of filamentous AIM2^{PYD} and ASC^{PYD}. Taken together, we assume that monomeric NLRP9^{PYD} already exists in a conformation compatible with filament formation. Since NLRP3^{PYD} showed the highest sequence identity with NLRP9^{PYD}, we also compared the conformations of both monomers (Figure 3F). Interestingly, they superimposed to RMSD of 1.0 Å and the structure of NLRP3^{PYD} closely resembled NLRP9^{PYD}. Therefore, NLRP9^{PYD} and NLRP3^{PYD} are not only related by sequence but also by conformation.

NLRP9^{PYD} does not self-polymerize nor nucleate ASC speck formation in HEK293T cells

As our structural analysis did not reveal any characteristic of NLRP9^{PYD} conclusively explaining its inability to form filaments *in vitro*, we set out to validate its behavior in the more physiological setting of HEK293T cells by overexpressing human NLRP9^{PYD} as mCitrine fusion protein. For comparison, we also overexpressed NLRP3^{PYD} fusion protein as the closest relative forming filaments. Similar to what was demonstrated by Stutz et al[14], in average 58.5 ± 4.7% of cells overexpressing NLRP3^{PYD}-mCitrine displayed large filaments with ring-shaped morphology (Figure 4A, B). In contrast, protein was found to diffusively locate within cells overexpressing NLRP9^{PYD}-mCitrine or mCitrine control under otherwise identical experimental conditions (Figure 4A). Significantly, no cells with filaments could be detected, thereby supporting our *in vitro* findings (Figure 2, 4B). Since NLRP9-dependent inflammasomes have been studied more extensively in the murine system[20–22], we also tested filament formation for murine NLRP9b^{PYD} fusion protein overexpressed in HEK293T cells. Given its relatively low sequence identity of 52.1% with human NLRP9^{PYD} (murine 1-91 versus human 1-94), we found it reasonable to anticipate murine NLRP9^{PYD} to potentially form filaments. Interestingly, we could not detect any filaments when overexpressing murine NLRP9^{PYD} in HEK293T cells, similarly as observed for human NLRP9^{PYD} (Figure 4A, B).

In contrast, many ASC-dependent inflammasomes studied so far displayed filament formation of the pyrin effector domain[13–15] and for NLRP3 it was also shown that mutations in its pyrin domain not only abrogated filament formation but also nucleation of ASC specks[14]. However, the ASC-dependent pyrin[45] or NLRP12[46–48] inflammasomes are examples where no hints for filament formation of their respective effector domains were found. We therefore investigated the ability of NLRP9^{PYD} to nucleate ASC speck formation regardless of filament formation. To this end, the fusion proteins were overexpressed in HEK293T cells stably expressing ASC-BFP (HEK293T$^{ASC\text{-}BFP}$). First, we analyzed whether presence of ASC has any effects on filament formation and found no significant difference in the number of cells with filaments between HEK293T and HEK293T$^{ASC\text{-}BFP}$ cells (Figure 4A, B). But interestingly, NLRP3^{PYD}-mCitrine filaments changed to a more star-like morphology with its centers co-

localizing with ASC specks (Figure 4A). Indeed, the number of cells with filaments (65.1 ± 7.4%, Figure 4B) clearly correlated with the number of cells that formed ASC specks (64.6 ± 4.8%, Figure 4C), which differed significantly from mCitrine control cells (2.1 ± 0.3%, Figure 4C). Importantly, when overexpressing human NLRP9^{PYD} or murine NLRP9b^{PYD}, the amounts of specking cells did not change significantly from the mCitrine control (Figure 4C).

To further investigate the differences between NLRP3 and NLRP9 and their impacts on filament formation and nucleation of ASC specks, we modelled one ring of the human NLRP3^{PYD} filament and a hypothetical filament slice of human NLRP9^{PYD} on the basis of the NLRP6^{PYD} filament structure[15] and used these to calculate APBS[49]-generated surface electrostatics (Figure 4D). Although it is hardly possible to predict behavior from the electrostatic surfaces of proteins, it is apparent that many charged clusters in NLRP3^{PYD} are found to be inversed in NLRP9^{PYD} (Figure 4D). As assumed previously, such charge inversions or insertions might disrupt intra- and inter-strand interactions, since clusters of similar charge would come close in a potential NLRP9^{PYD} filament (Figure 4D, NLRP9^{PYD} top and bottom views). Additionally, Lys48 and Lys49 of different subunits would center at the inner core ring in the hypothetical NLRP9^{PYD} filament (Figure 4D), which might cause strong repulsive forces, that are potentially not overcome by intra- and inter-strand interactions and thereby would prohibit formation of a filament. Since we do not know the exact molecular mechanism of how nucleation of ASC specks is facilitated by pyrin domain filaments, hypotheses about NLRP9-dependent ASC speck formation are highly speculative. But considering our model would resemble an effectively formed NLRP9^{PYD} filament, we were unable to find charge matching surface patches at interfacing positions (Figure 4D), thereby not excluding, *e.g.*, potential hydrophobic interactions between NLRP9 and ASC pyrin domains. However, those findings are of rather low evidence and further research revealing the molecular mechanisms that effectively prevent filament formation and nucleation of ASC specks would be needed for definite conclusions.

Discussion

At present, there is only limited knowledge about the details of NLRP inflammasome assembly. Evidenced by structural studies of the NAIP/NLRC4 inflammasome[50–53], the topologically conserved NACHT and LRR domains are presumed to adopt a closed and inactive conformation and transit upon activation into an open conformation allowing for oligomerization and successive signal transduction. Such oligomerization events might include homotypic filament formation of

then accessible pyrin domains, as demonstrated by cellular and structural studies of NLRP3[14] and NLRP6[15]. For NLRP6 it was additionally shown that such filaments in turn were sufficient to nucleate ASC polymerization[15]. We found that also in case of NLRP3, pyrin domain filaments are sufficient nucleators of ASC specks (Figure 4A). Yet, in contrast to NLRP3, our data also suggests that murine and human NLRP9^{PYD} does not self-polymerize into filaments, nor nucleate ASC speck formation in cells. This finding is contradictory with a previous study, showing NLRP9 to form an active inflammasome upon infection with rotavirus in the murine and human system[21]. Instead, our findings are reminiscent of a recent study on NLRP11, which was also shown to not interact with ASC but rather to repress NF-κB and type I interferon responses, two key innate immune pathways involved in inflammation[54].

Using X-ray crystallography, we determined the structure of human NLRP9^{PYD} and analyzed its characteristics on a molecular basis. We identified hydrophobic core residues to substantially stabilize the typical death domain fold of NLRP9^{PYD}, which are, in terms of hydrophobicity, conserved among the NLRP subfamily (Figure 3A). Additionally, we found a second hydrophobic cluster stabilizing the flexible α2-α3 loop region and thereby partially determining the conformation of NLRP9^{PYD}. Upon filament formation, NLRP6^{PYD} was shown to undergo large conformational changes especially in the α2-α3 loop region[15]. Our data instead support the hypothesis that the conformation of monomeric NLRP9^{PYD} and NLRP3^{PYD} is already compatible with filament formation with respect to the α2-α3 loop and the conformation of the C-terminal helix. Therefore, we assume that the inability of NLRP9^{PYD} to form filaments might not result from conformational restraints. Several residues were identified in comparison to filament forming pyrin domains, which are charge-inversed in NLRP9^{PYD} and typically positioned on otherwise interface surfaces. The primarily basic character of the hypothetical NLRP9^{PYD} filament inner core might cause repulsive forces that are not compensated by interfacing residues matching in charge, such that they most likely disrupt filament formation (Figure 4D). To validate this hypothesis, extensive mutational studies would be needed that will conclusively show this relationship.

In a previous study of the NLRP14^{PYD}, a cluster of three sites on the pyrin domain was identified, described as the Glu–Arg–Asp charge relay, that stabilizes the assembly between helices α2 and α6 and the loop preceding α6 through salt bridge formation[55]. This pattern of charged residues is contained in the PYDs of NLRP3 and NLRP9 (E22–R81–D83) but not in NLRP14 were the central arginine is found to be a leucine. Accordingly, the loose coordination of α6 in NLRP14^{PYD} allows for the formation of a long α5-α6 stem helix that leads to a concentration dependent monomer-to-dimer transition of the PYD. Our observation of a completely monomeric behavior of NLRP9^{PYD} is in accordance with these descriptions and the stability of the PYD domain, although it does not explain its inability to form filaments.

Post-translational modifications (PTMs) were found to be a common mechanism for the regulation of inflammasomes[56] and other PRRs[57]. The ability of NLRP3^{PYD} to form filaments is regulated by a single phosphorylation on Ser5, which prevents its oligomerization[14]. In turn, phosphorylation of Ser198 in NLRP3 was shown to be a pre-requisite for activation[58], indicating the delicate balance of inhibition and activation by PTM regulation. For NLRP9^{PYD}, a single phosphorylation could turn the basic, repulsive core of the estimated filament into an associative interaction. Likewise, regulative interaction partners of NLRP9 might be missing in our experimental setup using recombinant proteins. For instance, Zhu et al. described the RNA-helicase DHX9 as a potential interaction partner of NLRP9 during infection of intestinal epithelial cells (IECs) with rotavirus, yet without investigating the detailed interacting domains[21]. We used HEK293T cells for our experiments, which are known to express DHX9, but potentially co-transfection of certain RNA might be necessary to stimulate the interaction with NLRP9^{PYD}. To exclude the need of further interaction partners not expressed in HEK293T cells, filament formation of NLRP9^{PYD} could be tested in organoid cultures of IECs. It is also possible that the pyrin domain of NLRP9 is not involved in oligomerization and active inflammasome formation. Alternatively, synergism with the NACHT or LRR domains might be needed to effectively form filaments. However, previous studies on different inflammasome effector domains[13,9,15] as well as our own findings on NLRP3^{PYD} showed their sufficiency in filament formation and inflammasome activation and thus argue against this hypothesis.

In summary, the mechanisms of NLRP9 inflammasome formation remain largely unknown. If filament formation of effector domains is a hallmark of active inflammasomes, it must be tightly regulated in NLRP9 and further research elucidating its molecular mechanisms would be valuable to enable strategies for therapeutic intervention in diseases associated with its dysregulation.

Acknowledgments

We would like to thank the beamline scientists at Swiss Light Source (Villigen) and Deutsches Elektronen Synchrotron (Hamburg) for support. We also thank Dr. Gabor Horvath from the core facility microscopy in Bonn and Tomasz Próchnicki for support with imaging of cells. M.G. and E.L. are funded by the Deutsche Forschungsgemeinschaft (DFG, German Research Foundation) under Germany's Excellence Strategy – EXC2151–390873048. This work was supported by a grant from the Else Kröner-Fresenius-Stiftung to M.G. (2014_A203).

References

1. Xue, Y., Enosi Tuipulotu, D., Tan, W. H., Kay, C. & Man, S. M. Emerging Activators and Regulators of Inflammasomes and Pyroptosis. *Trends Immunol.* **40**, 1035–1052 (2019).
2. Kufer, T. A. & Sansonetti, P. J. NLR functions beyond pathogen recognition. *Nat. Immunol.* **12**, 121–128 (2011).
3. Yin, Q., Fu, T.-M., Li, J. & Wu, H. Structural Biology of Innate Immunity. *Annu. Rev. Immunol.* **33**, 393–416 (2015).
4. Mariathasan, S. *et al.* Differential activation of the inflammasome by caspase-1 adaptors ASC and Ipaf. *Nature* **430**, 213–218 (2004).
5. Man, S. M. & Kanneganti, T.-D. Converging roles of caspases in inflammasome activation, cell death and innate immunity. *Nat. Rev. Immunol.* **16**, 7–21 (2016).
6. Shi, J. *et al.* Cleavage of GSDMD by inflammatory caspases determines pyroptotic cell death. *Nature* **526**, 660–665 (2015).
7. Lu, A. *et al.* Unified Polymerization Mechanism for the Assembly of ASC-Dependent Inflammasomes. *Cell* **156**, 1193–1206 (2014).
8. Lu, A. & Wu, H. Structural mechanisms of inflammasome assembly. *FEBS J.* **282**, 435–444 (2015).
9. Li, Y. *et al.* Cryo-EM structures of ASC and NLRC4 CARD filaments reveal a unified mechanism of nucleation and activation of caspase-1. *Proc. Natl. Acad. Sci.* **115**, 10845–10852 (2018).
10. Heid, M. E. *et al.* Mitochondrial Reactive Oxygen Species Induces NLRP3-Dependent Lysosomal Damage and Inflammasome Activation. *J. Immunol.* **191**, 5230–5238 (2013).
11. Muñoz-Planillo, R. *et al.* K+ Efflux Is the Common Trigger of NLRP3 Inflammasome Activation by Bacterial Toxins and Particulate Matter. *Immunity* **38**, 1142–1153 (2013).
12. Amores-Iniesta, J. *et al.* Extracellular ATP Activates the NLRP3 Inflammasome and Is an Early Danger Signal of Skin Allograft Rejection. *Cell Rep.* **21**, 3414–3426 (2017).
13. Lu, A. *et al.* Plasticity in PYD assembly revealed by cryo-EM structure of the PYD filament of AIM2. *Cell Discov.* **1**, 15013 (2015).
14. Stutz, A. *et al.* NLRP3 inflammasome assembly is regulated by phosphorylation of the pyrin domain. *J. Exp. Med.* **214**, 1725–1736 (2017).
15. Shen, C. *et al.* Molecular mechanism for NLRP6 inflammasome assembly and activation. *Proc. Natl. Acad. Sci.* **116**, 2052–2057 (2019).
16. Dalbiès-Tran, R., Papillier, P., Pennetier, S., Uzbekova, S. & Monget, P. Bovine mater-like NALP9 is an oocyte marker gene. *Mol. Reprod. Dev.* **71**, 414–421 (2005).

17. Ponsuksili, S. *et al.* Bovine NALP5, NALP8, and NALP9 Genes: Assignment to a QTL Region and the Expression in Adult Tissues, Oocytes, and Preimplantation Embryos. *Biol. Reprod.* **74**, 577–584 (2006).
18. Thélie, A. *et al.* Differential regulation of abundance and deadenylation of maternal transcripts during bovine oocyte maturation in vitro and in vivo. *BMC Dev. Biol.* **7**, 125 (2007).
19. Romar, R. *et al.* Expression of Maternal Transcripts During Bovine Oocyte In Vitro Maturation is Affected by Donor Age: Gene Expression in Different Bovine Competence Models. *Reprod. Domest. Anim.* **46**, e23–e30 (2011).
20. Ngo, C. & Man, S. M. NLRP9b: a novel RNA-sensing inflammasome complex. *Cell Res.* **27**, 1302–1303 (2017).
21. Zhu, S. *et al.* Nlrp9b inflammasome restricts rotavirus infection in intestinal epithelial cells. *Nature* **546**, 667–670 (2017).
22. Yanling, Q. *et al.* Inhibition of NLRP9b attenuates acute lung injury through suppressing inflammation, apoptosis and oxidative stress in murine and cell models. *Biochem. Biophys. Res. Commun.* **503**, 436–443 (2018).
23. Nagyőszi, P. *et al.* Regulation of NOD-like receptors and inflammasome activation in cerebral endothelial cells. *J. Neurochem.* **135**, 551–564 (2015).
24. Nyúl-Tóth, Á. *et al.* Expression of pattern recognition receptors and activation of the non-canonical inflammasome pathway in brain pericytes. *Brain. Behav. Immun.* **64**, 220–231 (2017).
25. Tadaki, H. *et al.* De novo 19q13.42 duplications involving NLRP gene cluster in a patient with systemic-onset juvenile idiopathic arthritis. *J. Hum. Genet.* **56**, 343–347 (2011).
26. Castaño-Rodríguez, N., Kaakoush, N. O., Goh, K.-L., Fock, K. M. & Mitchell, H. M. The NOD-Like Receptor Signalling Pathway in Helicobacter pylori Infection and Related Gastric Cancer: A Case-Control Study and Gene Expression Analyses. *PLoS ONE* **9**, e98899 (2014).
27. Poli, G. *et al.* Expression of inflammasome-related genes in bladder cancer and their association with cytokeratin 20 messenger RNA. *Urol. Oncol. Semin. Orig. Investig.* **33**, 505.e1-505.e7 (2015).
28. Mearini, E. *et al.* Expression of urinary miRNAs targeting NLRs inflammasomes in bladder cancer. *OncoTargets Ther.* **Volume 10**, 2665–2673 (2017).
29. Poli, G. *et al.* Characterization of inflammasome-related genes in urine sediments of patients receiving intravesical BCG therapy. *Urol. Oncol. Semin. Orig. Investig.* **35**, 674.e19-674.e24 (2017).
30. Fernández, M. V. *et al.* Evaluation of Gene-Based Family-Based Methods to Detect Novel

Genes Associated With Familial Late Onset Alzheimer Disease. *Front. Neurosci.* **12**, 209 (2018).
31. Gil-Varea, E. *et al.* Exome sequencing study in patients with multiple sclerosis reveals variants associated with disease course. *J. Neuroinflammation* **15**, 265 (2018).
32. Page, R. *et al.* Shotgun crystallization strategy for structural genomics: an optimized two-tiered crystallization screen against the *Thermotoga maritima* proteome. *Acta Crystallogr. D Biol. Crystallogr.* **59**, 1028–1037 (2003).
33. Kabsch, W. Automatic processing of rotation diffraction data from crystals of initially unknown symmetry and cell constants. *J. Appl. Crystallogr.* **26**, 795–800 (1993).
34. Rossmann, M. G. The molecular replacement method. *Acta Crystallogr. A* **46**, 73–82 (1990).
35. Read, R. J. Pushing the boundaries of molecular replacement with maximum likelihood. *Acta Crystallogr. D Biol. Crystallogr.* **57**, 1373–1382 (2001).
36. Eibl, C. *et al.* Structural and Functional Analysis of the NLRP4 Pyrin Domain. *Biochemistry* **51**, 7330–7341 (2012).
37. Adams, P. D. *et al. PHENIX* : building new software for automated crystallographic structure determination. *Acta Crystallogr. D Biol. Crystallogr.* **58**, 1948–1954 (2002).
38. Emsley, P. & Cowtan, K. *Coot* : model-building tools for molecular graphics. *Acta Crystallogr. D Biol. Crystallogr.* **60**, 2126–2132 (2004).
39. DeLano, W. L. *The PyMOL Molecular Graphics System*. (DeLano Scientific, San Carlos, CA, USA, 2002).
40. McQuin, C. *et al.* CellProfiler 3.0: Next-generation image processing for biology. *PLOS Biol.* **16**, e2005970 (2018).
41. Ferrao, R. & Wu, H. Helical assembly in the death domain (DD) superfamily. *Curr. Opin. Struct. Biol.* **22**, 241–247 (2012).
42. Hiller, S. *et al.* NMR Structure of the Apoptosis- and Inflammation-Related NALP1 Pyrin Domain. *Structure* **11**, 1199–1205 (2003).
43. Bae, J. Y. & Park, H. H. Crystal Structure of NALP3 Protein Pyrin Domain (PYD) and Its Implications in Inflammasome Assembly. *J. Biol. Chem.* **286**, 39528–39536 (2011).
44. Pinheiro, A. S. *et al.* Three-dimensional Structure of the NLRP7 Pyrin Domain: INSIGHT INTO PYRIN-PYRIN-MEDIATED EFFECTOR DOMAIN SIGNALING IN INNATE IMMUNITY. *J. Biol. Chem.* **285**, 27402–27410 (2010).
45. Schnappauf, O., Chae, J. J., Kastner, D. L. & Aksentijevich, I. The Pyrin Inflammasome in Health and Disease. *Front. Immunol.* **10**, 1745 (2019).
46. Wang, L. *et al.* PYPAF7, a Novel PYRIN-containing Apaf1-like Protein That Regulates Activation of NF-κB and Caspase-1-dependent Cytokine Processing. *J. Biol. Chem.* **277**,

29874–29880 (2002).
47. Vladimer, G. I. *et al.* The NLRP12 Inflammasome Recognizes Yersinia pestis. *Immunity* **37**, 96–107 (2012).
48. Jin, T., Huang, M., Jiang, J., Smith, P. & Xiao, T. S. Crystal structure of human NLRP12 PYD domain and implication in homotypic interaction. *PLOS ONE* **13**, e0190547 (2018).
49. Jurrus, E. *et al.* Improvements to the APBS biomolecular solvation software suite: Improvements to the APBS Software Suite. *Protein Sci.* **27**, 112–128 (2018).
50. Hu, Z. *et al.* Crystal Structure of NLRC4 Reveals Its Autoinhibition Mechanism. *Science* **341**, 172–175 (2013).
51. Diebolder, C. A., Halff, E. F., Koster, A. J., Huizinga, E. G. & Koning, R. I. Cryoelectron Tomography of the NAIP5/NLRC4 Inflammasome: Implications for NLR Activation. *Structure* **23**, 2349–2357 (2015).
52. Hu, Z. *et al.* Structural and biochemical basis for induced self-propagation of NLRC4. *Science* **350**, 399–404 (2015).
53. Zhang, L. *et al.* Cryo-EM structure of the activated NAIP2-NLRC4 inflammasome reveals nucleated polymerization. *Science* **350**, 404–409 (2015).
54. Ellwanger, K. *et al.* The NLR family pyrin domain–containing 11 protein contributes to the regulation of inflammatory signaling. *J. Biol. Chem.* **293**, 2701–2710 (2018).
55. Eibl, C., Hessenberger, M., Wenger, J. & Brandstetter, H. Structures of the NLRP14 pyrin domain reveal a conformational switch mechanism regulating its molecular interactions. *Acta Crystallogr. D Biol. Crystallogr.* **70**, 2007–2018 (2014).
56. Yang, J., Liu, Z. & Xiao, T. S. Post-translational regulation of inflammasomes. *Cell. Mol. Immunol.* **14**, 65–79 (2017).
57. Liu, J., Qian, C. & Cao, X. Post-Translational Modification Control of Innate Immunity. *Immunity* **45**, 15–30 (2016).
58. Song, N. *et al.* NLRP3 Phosphorylation Is an Essential Priming Event for Inflammasome Activation. *Mol. Cell* **68**, 185–197 (2017).

Table 1: Crystallographic data collection and refinement statistics.

Data collection	
Space group	$P6_522$
a, b, c (Å)	33.33, 33.33, 311.09
Resolution (Å) [a]	28.74–1.95 (2.02–1.95)
R_{merge} (%)	8.25 (98.49)
I/σ (I)	18.58 (1.84)
Completeness (%)	99.52 (99.23)
$CC_{1/2}$	0.998 (0.916)
Redundancy	22.3 (16.7)
Refinement	
Resolution (Å)	28.74–1.95
No. reflections	14097
R_{work}/R_{free} [b]	0.215/0.222
No. atoms	
Protein	772
Water	17
B-factors	
Protein	68.96
Water	75.60
R.m.s deviations	
Bond lengths (Å)	0.006
Bond angles (°)	0.74
Residues in Ramachandran	
Favored regions (%)	98.86
Allowed regions (%)	1.14
PDB	
Accession number	6Z2G

[a] Values in parentheses are for the highest resolution shell.

[b] R_{free}-value is equivalent to the R-value but is calculated for 5% of the reflections chosen at random and omitted from the refinement process.

Figure Legends

Figure 1: Crystal structure of the human NLRP9 pyrin domain. (**A**) Cartoon of the human NLRP9 domain architecture. (**B**) Cartoon representation of the NLRP9^{PYD} crystal structure with six antiparallel helices and long α2-α3 loop, surrounded by detailed views of the respective residues fitted into the electron density map ($2F_o$-F_c map contoured at 1.0 sigma). (**C**) Color-coded electrostatic surface representation of NLRP9^{PYD} generated with APBS[49]. Unit of the scale is k_BT/e_c. (**D**) Plot of individual B factors for each residue of NLRP9^{PYD}. Values for backbone (blue) and sidechains (red) were calculated separately. Sidechains without occupancy were excluded. Secondary structure elements of NLRP9^{PYD} are plotted above the corresponding residue numbers. (**E**) Bottom view of NLRP9^{PYD} (magnified and rotated by 90° about the x axis relative to B). Hydrophobic core residues stabilizing the six-helical fold in NLRP9^{PYD} are shown as pink sticks. A second hydrophobic cluster stabilizing the α2-α3 loop is shown as green sticks.

Figure 2: Molecular dispersion of recombinant NLRP9^{PYD}. (**A**) Hydrodynamic radius and corresponding molecular weight of NLRP9^{PYD} as determined by DLS. Sample was measured every 30 minutes during 11.5 h of incubation at 25°C. Data points are representative of three independent experiments. n = 3 ± SEM. (**B**) Representative elution profile from analytical size exclusion chromatography of NLRP9^{PYD} before and after 12 h of incubation time at 25°C. The void volume (v_0) and total volume (v_t) of the column are depicted as arrows. (**C**) Calculation of the molecular weight of NLRP9^{PYD} from the peak retention volume obtained by analytical size exclusion chromatography. The calibration curve was plotted using the partition coefficient (K_{av}) versus the logarithm of the molecular weight of a standard. Data points are representative of three independent experiments. n = 3 ± SEM.

Figure 3: Structural comparison of NLRP9^{PYD} with filament forming pyrin domains. (**A**) Structure-based sequence alignment of the PYD of NLRP9 and the filament forming PYDs of NLRP3, NLRP6, AIM2 and ASC. Asp8 was included in the alignment, since density of the mainchain could be seen at lower sigma level. For NLRP6, AIM2 and ASC the filament structures are known and the residues forming the asymmetric interfaces are highlighted with the indicated colors. Residues that form the hydrophobic core of NLRP9^{PYD} are shown in yellow boxes. Secondary structure elements of NLRP9^{PYD} are plotted above the corresponding sequence. (**B**) Chart of three flanking subunits in a typical PYD filament. They form unified type I, type II, and type III interfaces. Subunits are labelled lightblue, lightgreen and

lightmagenta. (**C**) Overlay of the NLRP9^{PYD} crystal structure with the MBP-NLRP6^{PYD} crystal structure (6NDJ, chain A) and the NLRP6^{PYD} filament structure (6NCV). (**D**) Overlay of NLRP9^{PYD} with the MBP-AIM2^{PYD} crystal structure (3VD8) and the GFP-AIM2^{PYD} filament structure (6MB2). (**E**) Overlay of NLRP9^{PYD} with the monomeric ASC^{PYD} structure (1UCP) and the ASC^{PYD} filament structure (3J63). (**F**) Structural comparison of the NLRP9^{PYD} crystal structure with the NLRP3^{PYD} crystal structure (3QF2, chain A).

Figure 4: Analysis of PYD polymerization and ASC speck formation in cells. (**A**) Images of indicated mCitrine fusion proteins overexpressed in HEK293T or HEK293T$^{ASC\text{-}BFP}$ cells. (*) Plasmid coding for mCitrine-HA was transfected as a control and due to IRES expression had to be imaged with higher exposure time. Bar, 10 µm. Images are representative of three independent experiments. (**B**) Quantification of mCitrine positive cells with filaments. Bars are representative of three independent experiments. n = 3 ± SEM; ****, P < 0.0001 (two-way ANOVA followed by Holm-Sidak's multiple comparisons test). (**C**) Quantification of mCitrine positive cells with ASC speck. Bars are representative of three independent experiments. n = 3 ± SEM; ****, P < 0.0001 (ordinary one-way ANOVA followed by Holm-Sidak's multiple comparisons test). (**D**) Color-coded electrostatic surface representation of subunits of NLRP9^{PYD} and filament slices of NLRP3^{PYD}, ASC^{PYD}, and NLRP9^{PYD} generated with APBS[49]. The filament slice of ASC^{PYD} was adapted from the ASC^{PYD} filament structure (3J63). Crystal structures of monomeric NLRP3^{PYD} (3QF2) and NLRP9^{PYD} were used to model slice representations of a NLRP3^{PYD} filament and a hypothetical NLRP9^{PYD} filament. Modelling was based on the filament structure of NLRP6^{PYD} (6NCV). Bottom views represent a superjacent slice of the respective filament, that was rotated by 180° about the y-axis and mirrored horizontally to show interfacing regions in the filament at the same x/y coordinates of top and bottom views. Unit of the scale is k_BT/e_c.

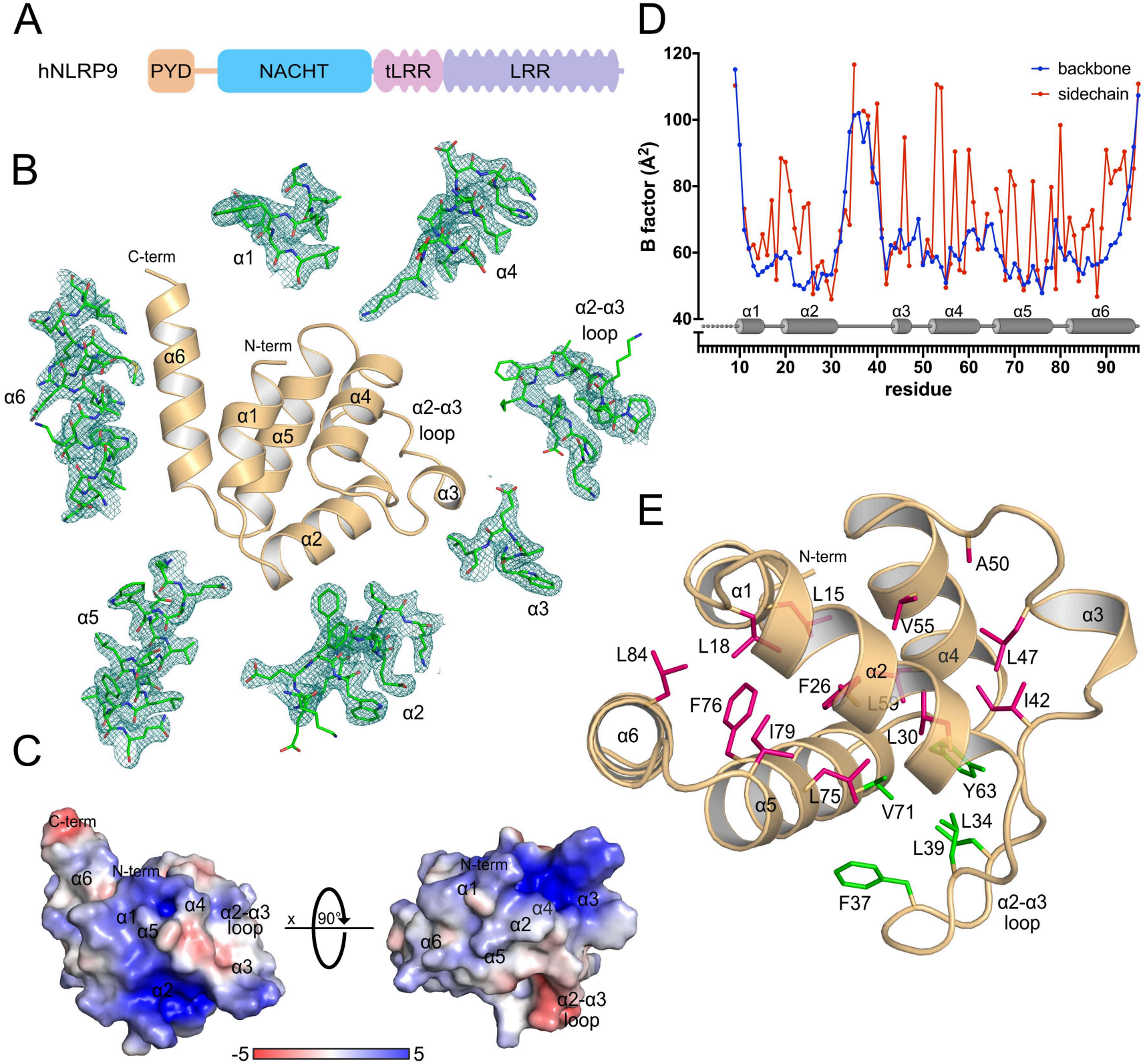
A
hNLRP9
PYD
NACHT
tLRR
LRR
B
C-term
α1
α4
α6
N-term
α2-α3
loop
α5
α3
α2
C
C-term
N-term
α6
α1
α5
α4
α2-α3
loop
α3
α2
x
90°
-5
5
D
backbone
sidechain
B factor (Å²)
120
100
80
60
40
α1
α2
α3
α4
α5
α6
10
20
30
40
50
60
70
80
90
residue
E
N-term
A50
α1
L15
V55
α3
L18
L84
α4
L47
α2
F26
F76
I42
α6
I79
L30
Y63
α5
L75
V71
L34
L39
F37
α2-α3
loop

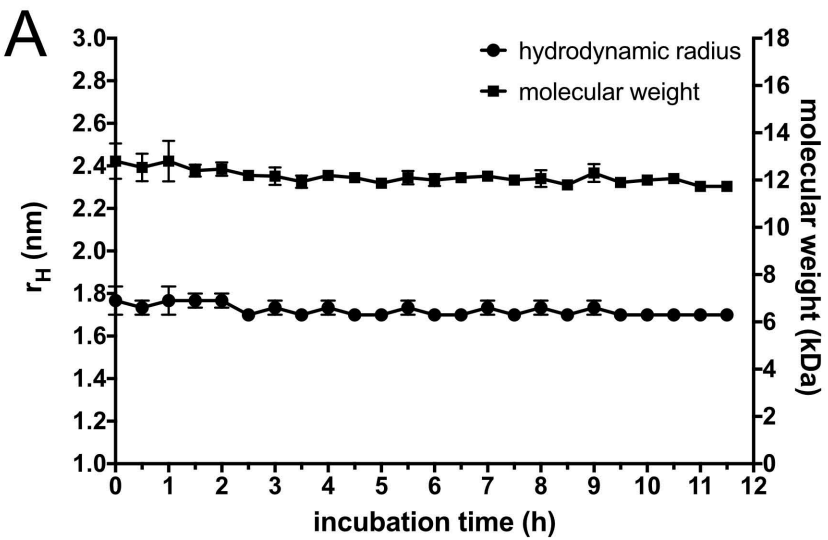
A
hydrodynamic radius
molecular weight
r_H (nm)
molecular weight (kDa)
incubation time (h)

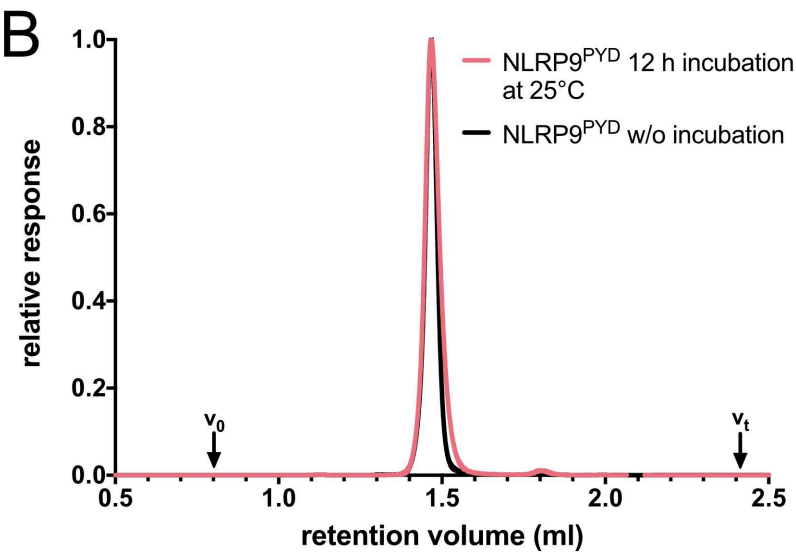
B
NLRP9PYD 12 h incubation at 25°C
NLRP9PYD w/o incubation
relative response
v_0
v_t
retention volume (ml)

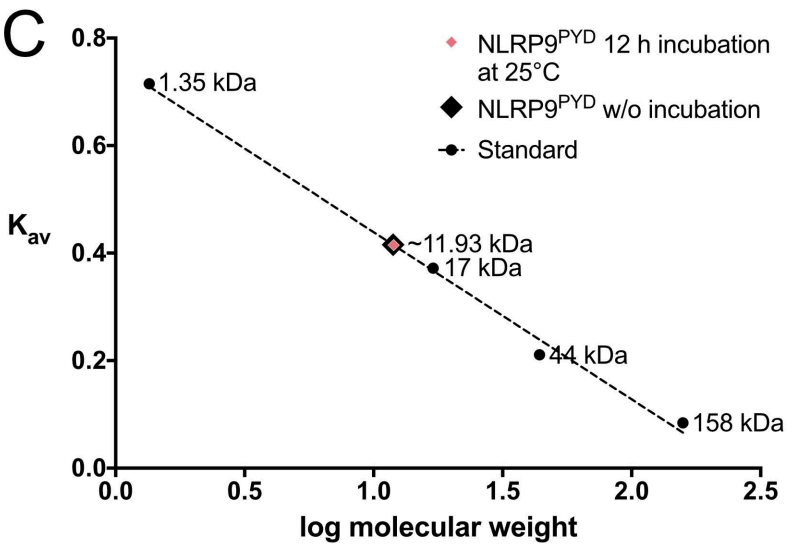
C
NLRP9PYD 12 h incubation at 25°C
NLRP9PYD w/o incubation
Standard
1.35 kDa
~11.93 kDa
17 kDa
44 kDa
158 kDa
K_{av}
log molecular weight

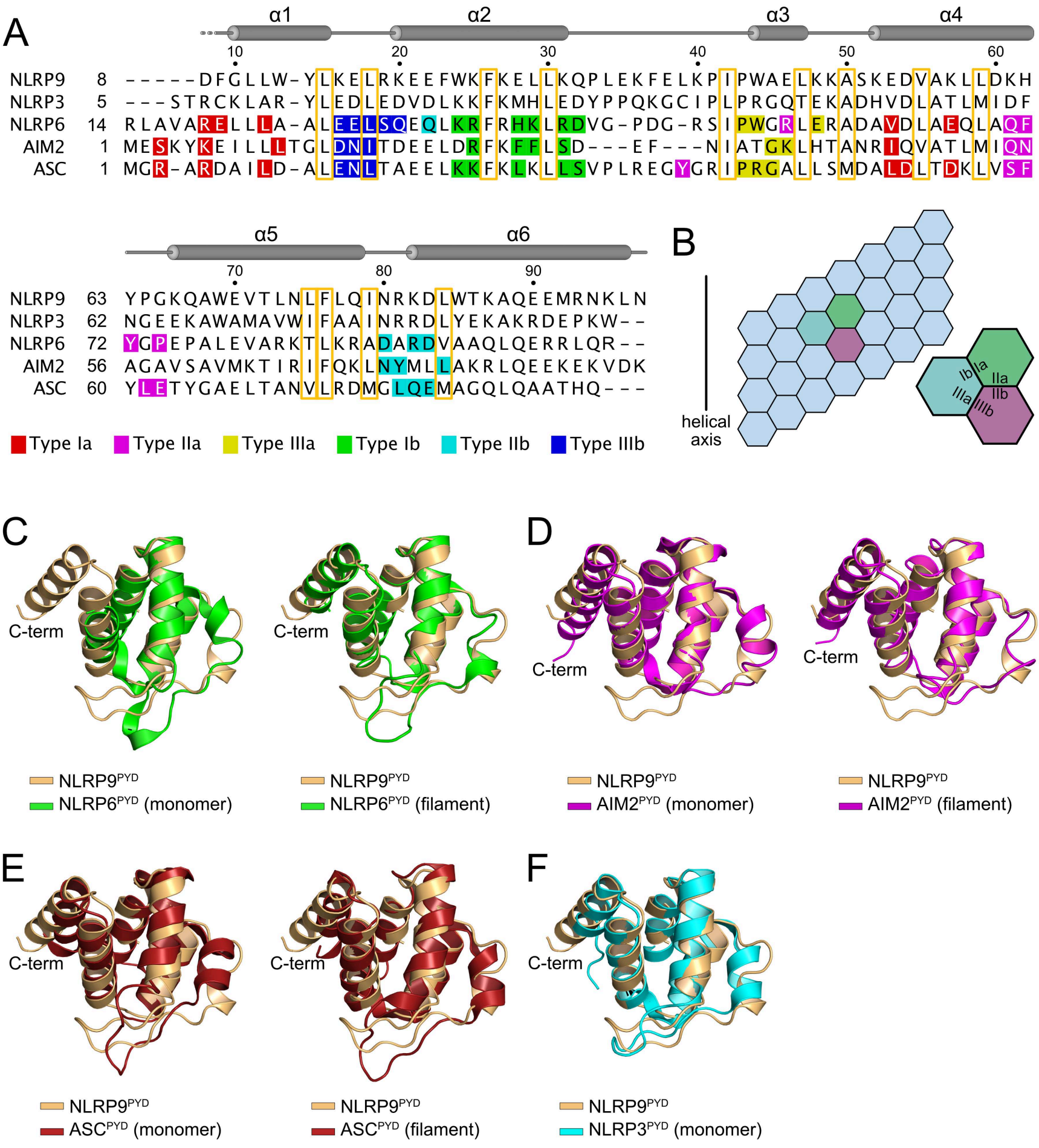
A
α1
α2
α3
α4
10
20
30
40
50
60
NLRP9 8 -----DFGLLW-YLKELRKEEFWKFKELLKQPLEKFELKPIPWAELKKASKEDVAKLLDKH
NLRP3 5 ---STRCKLAR-YLEDLEDVDLKKFKMHLEDYPPQKGCIPLPRGQTEKADHVDLATLMIDF
NLRP6 14 RLAVARELLLA-ALEELSQEQLKRFRHKLRDVG-PDG-RSIPWGRLERADAVDLAEQLAQF
AIM2 1 MESKYKEILLLTGLDNITDEELDRFKFFLSD---EF---NIATGKLHTANRIQVATLMIQN
ASC 1 MGR-ARDAILD-ALENLTAEELKKFKLKLLSVPLREGYGRIPRGALLSMDALDLTDKLVSF
α5
α6
70
80
90
NLRP9 63 YPGKQAWEVTLNLFLQINRKDLWTKAQEEMRNKLN
NLRP3 62 NGEEKAWAMAVWIFAAINRRDLYEKAKRDEPKW--
NLRP6 72 YGPEPALEVARKTLKRADARDVAAQLQERRLQR--
AIM2 56 AGAVSAVMKTIRIFQKLNYMLLAKRLQEEKEKVDK
ASC 60 YLETYGAELTANVLRDMGLQEMAGQLQAATHQ---
Type Ia
Type IIa
Type IIIa
Type Ib
Type IIb
Type IIIb
B
helical axis
Ia
Ib
IIa
IIb
IIIa
IIIb
C
C-term
C-term
NLRP9PYD
NLRP6PYD (monomer)
NLRP9PYD
NLRP6PYD (filament)
D
C-term
C-term
NLRP9PYD
AIM2PYD (monomer)
NLRP9PYD
AIM2PYD (filament)
E
C-term
C-term
NLRP9PYD
ASCPYD (monomer)
NLRP9PYD
ASCPYD (filament)
F
C-term
NLRP9PYD
NLRP3PYD (monomer)

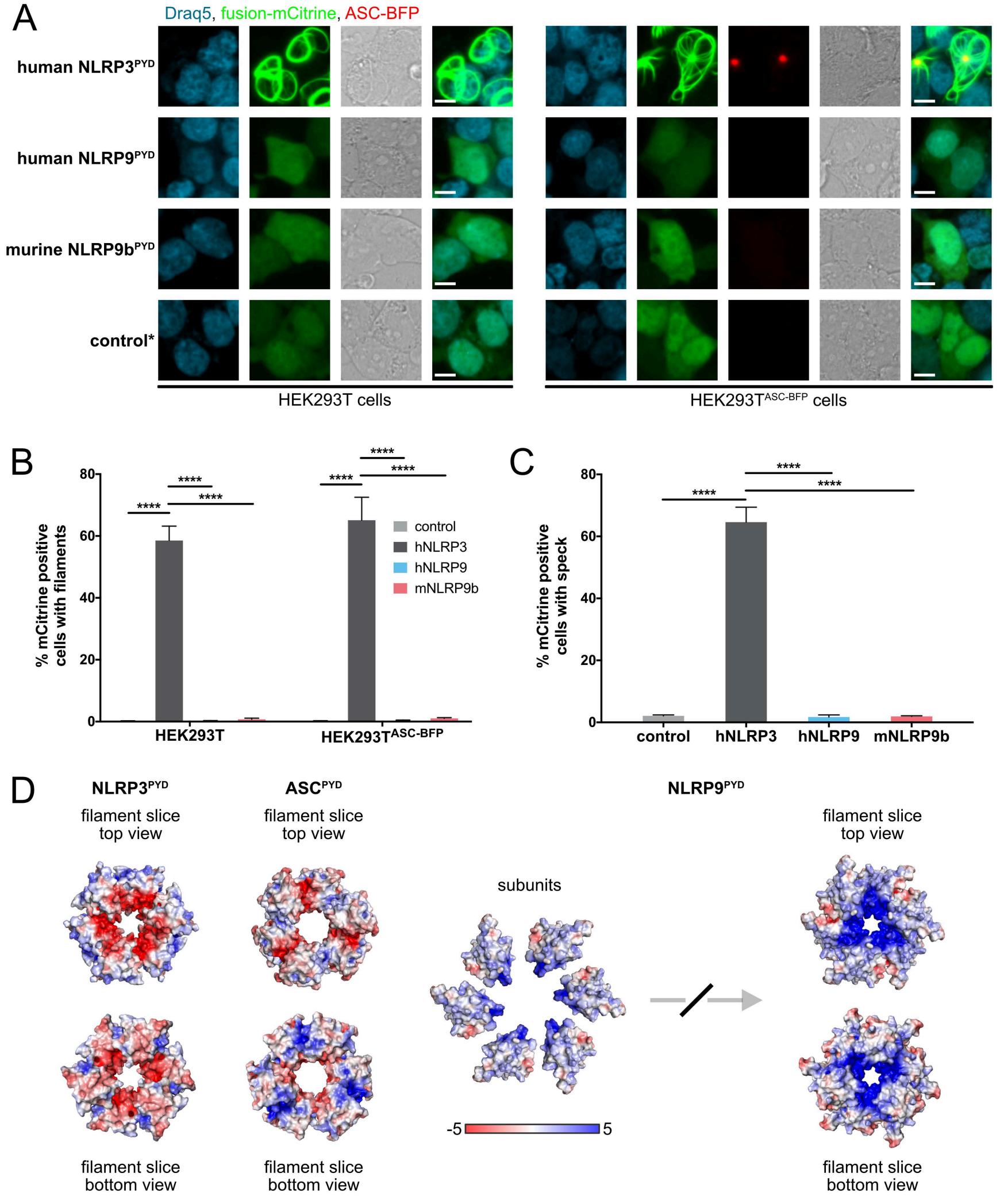
A
Draq5, fusion-mCitrine, ASC-BFP
human NLRP3PYD
human NLRP9PYD
murine NLRP9bPYD
control*
HEK293T cells
HEK293TASC-BFP cells
B
% mCitrine positive cells with filaments
control
hNLRP3
hNLRP9
mNLRP9b
HEK293T
HEK293TASC-BFP
C
% mCitrine positive cells with speck
control
hNLRP3
hNLRP9
mNLRP9b
D
NLRP3PYD
filament slice top view
ASCPYD
filament slice top view
NLRP9PYD
filament slice top view
subunits
-5
5
filament slice bottom view
filament slice bottom view
filament slice bottom view